Realistic transverse images of the proton charge and magnetization densities

Siddharth Venkat,[1,2] John Arrington,[3] Gerald A. Miller,[2,*] and Xiaohui Zhan[3]

[1]*Virginia Polytechnic Institute and State University, Blacksburg, Virginia 24061-0002, USA*
[2]*Department of Physics, University of Washington, Seattle, Washington 98195-1560, USA*
[3]*Physics Division, Argonne National Laboratory, Argonne, Illinois 60439, USA*

We develop a technique, denoted as the finite radius approximation (FRA), that uses a two-dimensional version of the Nyquist-Shannon sampling theorem to determine transverse densities and their uncertainties from experimental quantities. Uncertainties arising from experimental uncertainties on the form factors and lack of measured data at high Q^2 are treated. A key feature of the FRA is that a form factor measured at a given value of Q^2 is related to a definite region in coordinate space. An exact relation between the FRA and the use of a Bessel series is derived. The proton Dirac form factor is sufficiently well known such that the transverse charge density is very accurately known except for transverse separations b less than about 0.1 fm. The Pauli form factor is well known to Q^2 of about 10 GeV^2, and this allows a reasonable, but improvable, determination of the anomalous magnetic moment density.

I. INTRODUCTION

A truly impressive level of experimental technique, effort, and ingenuity has been applied to measuring the electromagnetic form factors of the proton, neutron (nucleon), and pion [1–6]. These quantities are probability amplitudes that a given hadron can absorb a specific amount of momentum and remain in the ground state, and therefore should supply information about charge and magnetization spatial densities.

The textbook interpretation of these form factors is that their Fourier transforms are measurements of the charge and magnetization densities. This interpretation is deeply buried in the thinking of nuclear physicists and continues to guide intuition, as it has since the days of the Nobel Prize–winning work of Hofstadter [7]. Nevertheless, the relativistic motion of the constituents of the system causes the textbook interpretation to be incorrect [8]. The difficulty is that in electron-proton scattering the initial and final nucleon states have different momenta and therefore different wave functions. In general, these different states are related by a boost operator that depends on the full complexity of QCD. The use of transverse densities [9,10] avoids this difficulty by working in the infinite momentum frame and taking the spacelike momentum transfer to be in the direction transverse to that of the infinite momentum. In this case, the different momenta of the initial and final nucleon states are accommodated by using two-dimensional Fourier transforms. The transverse charge and magnetization densities are constructed from density operators that are the absolute square of quark-field operators, so they are correctly defined as densities.

It is useful to note that the transverse densities are closely connected to generalized parton distributions (GPDs), which describe the distribution of quark and antiquarks with respect to longitudinal momentum and transverse position. The integral of the GPD H, evaluated at 0 skew, over longitudinal

momentum gives the transverse charge density of interest here [11,12].

In this paper, we are concerned with extracting the spatial information by developing and using a theoretical technique that is model independent and also provides a practical way of dealing with both experimental uncertainties and the lack of information on unmeasured regions, with minimal assumptions. In the subsequent text, we plan to show how to construct bands of transverse densities that are consistent with available experimental knowledge and also take into account the possible effects of data taken at momentum transfer Q^2 higher than available in the present data set. This allows one to consider the possible impact of future experiments.

There also is a more general context, with the high current interest in mapping the three-dimensional structure of the nucleon [13]. Therefore, we also aim to provide a technique that can be easily extended to determining the spatial aspects of other quantities [11,12] related to transverse momentum distributions and generalized parton distributions.

Next, we present an overview of the remainder of this paper. Section II concerns the following situation: Suppose a form factor $F(Q^2)$ and transverse density $\rho(b)$ are related by a two-dimensional Fourier transform and that $\rho(b)$ is localized, $\rho(b) = 0$ for b greater than some finite distance. The function $\rho(b)$ is band limited and can be written as a discrete Fourier series involving $F(Q^2)$. This result, known as the Nyquist-Shannon [14] sampling theorem, enables us to associate the density at a given range of values of b with a discrete value of the momentum transfer; see Eq. (3) (which we denote as the finite radius approximation, FRA). The equivalence between the FRA and the Bessel series expansion technique is also established. A general version of the FRA, applicable to other observable quantities, is also presented.

Section III is concerned with exploring the validity and utility (which depend on the number of terms needed in the discrete Fourier series) of the FRA using examples in which the form factor is given by a monopole (M) or dipole (D) form. Section V is concerned with the reality

---

*miller@phys.washington.edu

that the proton electromagnetic form factors are not known as analytic functions. Instead, form factors $G_{E,M}$, $F_{1,2}$ (with uncertainties) measured at discrete values of Q^2 up to a finite maximum value Q^2_{max} are known. This means that ρ is known only within some uncertainties, and a technique to determine the uncertainties in ρ must be developed. This is accomplished by using the values of $F_i \pm dF_i$ in the FRA. Estimates of the effects of incompleteness, arising from contributions in the unmeasured region, $Q^2 > Q^2_{max}$, are also provided. The paper is concluded with a brief summary.

II. GENERAL CONSIDERATIONS

Intuitively, we expect particles to be localized. That is, we expect densities associated with the particle to be well approximated by functions that are zero outside some maximum radius. This assumption, the FRA, greatly simplifies the relationship between form factors and their associated densities.

Let $\rho(b)$ be a two-dimensional transverse density function (we later take this to be charge or magnetization density), and let $F(Q^2)$ be the associated form factor. The transverse density is given by [9,15]

$$\rho(b) = \frac{1}{(2\pi^2)} \int d^2 q e^{-i\mathbf{q}\cdot\mathbf{b}} \, F(Q^2 = \mathbf{q}^2)$$
$$= \frac{1}{2\pi} \int Q dQ J_0(Qb) F(Q^2), \tag{1}$$

with the azimuthal symmetry of ρ obtained from the Lorentz invariant form of F in the spacelike region with $q^+ = 0$. If one knows $F(Q^2)$ exactly for all values of Q^2, the transverse density is known immediately. However, one knows $F(Q^2)$ only within experimental uncertainties for a finite range of Q^2. This means that ρ is known only within some uncertainties, and it is necessary to develop a technique to determine the uncertainties in ρ.

We proceed by assuming that $\rho(b) \approx 0$ for $b \geqslant R$, where R is a finite distance. Since the functions ρ, F are Fourier transforms, F is band limited. We proceed in the spirit of the Nyquist-Shannon sampling theorem. The function ρ can be expanded as

$$\rho(b) = \sum_{n=1}^{\infty} c_n J_0\left(X_n \frac{b}{R}\right), \tag{2}$$

where X_n is the nth zero of J_0 and c_n is given approximately by the formula

$$c_n \approx \widetilde{c}_n = \frac{1}{2\pi} \frac{2}{R^2 J_1(X_n)^2} F(Q_n^2), \tag{3}$$

with

$$Q_n \equiv \frac{X_n}{R}. \tag{4}$$

Equation (3), which is the two-dimensional version of Ref. [14], is the central formal result of this paper. Using

this in Eq. (2) yields the following expression for $\rho(b)$:

$$\rho(b) = \frac{1}{\pi R^2} \sum_{n=1}^{\infty} J_1(X_n)^{-2} F(Q_n^2) J_0\left(X_n \frac{b}{R}\right), \tag{5}$$

The result, Eq. (5), is the central phenomenological result because it tells us that measuring a form factor at Q_n^2 provides information about the density mainly at values of $b < R/X_n$. This is because Bessel functions are of the order of unity only for values of arguments less than that of its first zero.

A. Equivalence with the Bessel series

Replacing c_n by $\widetilde{c}_n$ would be exact if the assumption $\rho(b \geqslant R) = 0$ is exactly true. This condition is clearly approximately true, so we expect a near equality between c_n and $\widetilde{c}_n$. In fact, it turns out that the approximation is amazingly accurate, as we now demonstrate. Numerical examples are provided in subsequent sections. The exact values of c_n are obtained from the orthogonality of the cylindrical Bessel functions as

$$c_n = \frac{2}{R^2 J_1(X_n)^2} \int_0^R b\rho(b) J_0\left(X_n \frac{b}{R}\right) db. \tag{6}$$

The use of this in Eq. (1) followed by integration over b can be done using a standard identity to yield

$$c_n = \frac{X_n}{\pi R^2 J_1(X_n)} \int_0^{\infty} \frac{q F(q^2) J_0(qR)}{\left(\frac{X_n}{R}\right)^2 - q^2} dq. \tag{7}$$

We may use a dispersion relation for the form factor [16] to establish the connection between $\widetilde{c}_n$ and c_n. First, recall that, for $Q^2 > 0$,

$$F(Q^2) = \frac{1}{\pi} \int_{4m_\pi^2}^{\infty} dt \frac{\text{Im} F(-t)}{t + Q^2}, \tag{8}$$

and that using this expression in Eq. (1) yields

$$\rho(b) = \frac{1}{2\pi^2} \int_{4m_\pi^2}^{\infty} dt \, K_0(\sqrt{t}b) \text{Im} F(-t). \tag{9}$$

Proceed by using this in Eq. (6) and then integrate over b using

$$\int_0^R b db K_0(\sqrt{t}b) J_0\left(b \frac{X_n}{R}\right)$$
$$= \frac{1}{\frac{X_n^2}{R^2} + t} \times [1 + X_n J_1(X_n) K_0(\sqrt{t}R)]. \tag{10}$$

Then,

$$c_n = \frac{1}{R^2 J_1(X_n)^2 \pi^2} \int_{4m_\pi^2}^{\infty} dt \frac{\text{Im} F(-t)}{t + \frac{X_n^2}{R^2}}$$
$$\times [1 + X_n J_1(X_n) K_0(\sqrt{t}R)]. \tag{11}$$

Using only the first term within the brackets along with Eq. (8) allows one to identify the integral over t as $\pi F(Q_n^2)$. Thus [using Eq. (3)] one arrives at the result that $c_n = \widetilde{c}_n$ plus a correction term, suppressed by a modified Bessel function evaluated at a large argument. For example, a significant contribution to Im F comes from the region $t \sim m_\rho^2 = 0.5$ GeV^2,

and by using $R = 3.3$ fm (see Sec. III), $K_0(m_\rho R) = 10^{-6}$. The net result is that

$$c_n = \widetilde{c}_n + \delta_n,$$

$$\delta_n \equiv \frac{X_n R^2 J_1(X_n)}{J_1^2(X_n)\pi^2} \int_{4m_\pi^2}^\infty dt \frac{\mathrm{Im}F(-t)}{t + \frac{X_n^2}{R^2}} K_0(\sqrt{t}R). \quad (12)$$

A reasonable estimate is that

$$\frac{c_n - \widetilde{c}_n}{\widetilde{c}_n} \sim X_n J_1(X_n) 10^{-6}. \quad (13)$$

The condition that δ_n be small is so that R is chosen to be large enough. We ensure that this condition is satisfied for all of our examples and applications.

B. Preliminary evaluations

It is worthwhile to perform some preliminary analysis of the expression Eq. (5). For $x \gg 1$, $J_0(x)$ is well approximated [17] by

$$J_0(x) \approx \sqrt{\frac{2}{\pi x}} \cos\left(x - \frac{\pi}{4}\right), \quad (14)$$

so that the n'th zero of J_0, X_n, is given approximately by

$$X_n \approx \left(n + \tfrac{3}{4}\right)\pi, \quad (15)$$

and

$$\begin{aligned} J_1(X_n) &= -J_0'(X_n) \\ &\approx (-1)^n 2^{1/2}\pi^{-1}\left[\left(n + \tfrac{3}{4}\right)\right]^{-1/2}. \end{aligned} \quad (16)$$

It follows that for large n, the terms in the series Eq. (5) for $\rho(b)$ are of the form

$$\frac{\pi}{2R^2}\left(n + \frac{3}{4}\right)F\left(Q_n^2\right)J_0\left(X_n\frac{b}{R}\right) \sim n\, F\left[\left(\frac{n\pi}{R}\right)^2\right]$$

at $b = 0$. So for the series to converge everywhere, namely at $b = 0$, we need F to fall faster than Q^{-2} for large Q. The oscillations of the cylindrical Bessel functions hasten the convergence for nonzero values of b.

Given this convergence, the function $\rho(b)$ can be approximated by using a finite number of terms in the series Eq. (5). Because $Q_n^2 = (X_n/R)^2$ serves as the Q^2 in the argument of F, cutting off the series at N terms is equivalent to taking $F(Q^2) = 0$ for $Q^2 > (X_N/R)^2$.

If the assumption that $\rho(b) = 0$ for $b \geqslant R$ holds for a given value of R, then it also holds for larger values of R. We can see from Eq. (5) that increasing R increases the frequency with which $F(Q^2)$ is sampled and therefore decreases the range that is sampled. As a consequence, an increase in R demands an increase in the number of terms in the approximation for ρ.

A quick result following from the fact that ρ is the Fourier transform of F is that the mean square radius $\langle b^2 \rangle$ is given by

$$\langle b^2 \rangle \equiv \int d^2b \, b^2 \rho(b) = -4 \left.\frac{d\log F}{dQ^2}\right|_{Q^2=0}. \quad (17)$$

In this paper, we choose $R \approx 5\sqrt{|\langle b^2 \rangle|}$ in determining the number of terms in our expansion. Numerical studies of the

form factors considered in preparing this paper have shown that this value of R is sufficiently large so that perturbations to this value lead to the same density functions and that $R^2\rho(R)$ is always small enough so that the difference between c_n and $\widetilde{c}_n$ is minute.

C. Other transverse densities

We believe that the techniques used in this paper can be exploited to image other quantities that depend on transverse position. Suppose there is a transverse quantity $\rho^{(\lambda)}(b)$ that is a two-dimensional Fourier transform of an experimental observable $F^{(\lambda)}(Q^2)$ such that

$$\rho^{(\lambda)}(b) = \frac{1}{2\pi} \int Q\,dQ\,J_\lambda(Qb)F^{(\lambda)}(Q^2). \quad (18)$$

An example, discussed in detail in Sec. V C, is the magnetization density ρ_m of the anomalous magnetic moment. We expect that the index (λ) is associated with a given number of units of orbital angular momentum. Extracting $\rho^{(\lambda)}(b)$ is facilitated by using the expansion

$$\rho^{(\lambda)}(b) = \sum_{n=1}^\infty c_{n\lambda} J_\lambda\left(X_{\lambda,n}\frac{b}{R}\right), \quad (19)$$

where $X_{\lambda,n}$ is the nth zero of the Bessel function of order λ. Then the sampling theorem leads immediately to the result:

$$\begin{aligned} c_{n,\lambda} &\approx \widetilde{c}_{n,\lambda} = \frac{2}{R^2 J_{\lambda+1}(X_{\lambda,n})^2} F^{(\lambda)}\left(Q_{\lambda,n}^2\right), \\ Q_{\lambda,n} &= \frac{X_{\lambda,n}}{R}. \end{aligned} \quad (20)$$

The difference between $c_{n,\lambda}$ and $\widetilde{c}_{n,\lambda}$ can be shown to be very small by using the arguments of Sec. II A. The result, Eq. (20), can be used to relate accessible kinematic ranges with transverse regions.

III. EXAMPLES

To demonstrate our method and explore its limitations, we now analyze two models of the form factor. For the first model, let the form factor be given by the monopole form

$$F_{\mathrm{Mono}}(Q^2) = \frac{1}{1 + \frac{Q^2}{\Omega^2}}, \quad (21)$$

where $\Omega = 0.77$ GeV. This form factor is taken as a caricature of the pion electromagnetic form factor. Then the associated charge density is obtained from Eq. (1):

$$\rho_{\mathrm{Mono}}(b) = \frac{1}{2\pi}\Omega^2 K_0(\Omega b). \quad (22)$$

This function diverges as $\log(1/b)$ for small values of b and so provides a severe test of the method. With the stated value of Ω, we find $\langle b^2 \rangle_{\mathrm{Mono}} = 4/\Omega^2 = 0.26$ fm^2 and thus take $R = 5\sqrt{|\langle b^2 \rangle|} = 2.56$ fm. We then find the fractional difference between c_n and $\widetilde{c}_n$ of Eq. (12) is less than 5×10^{-4} for small values of n, and the magnitude decreases rapidly as n increases.
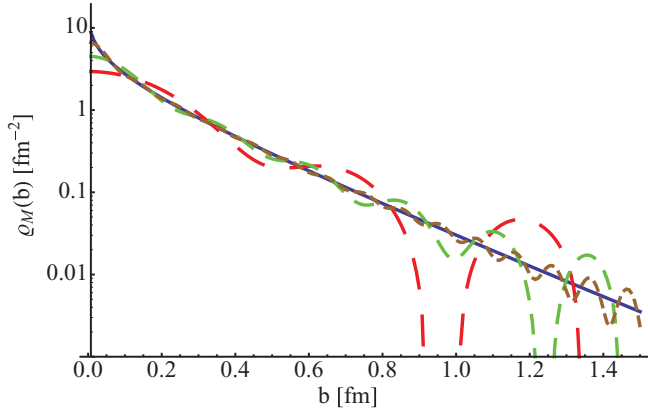
FIG. 1. (Color online) Plot of ρ_M (blue, solid), 10-term approximation (red, long dash), 20-term approximation (green, medium dash), and 50-term approximation (brown, short dash).

We compare to ρ_{Mono} to its approximation as an expansion in N terms, with $N = 10, 20, 50$ in Fig. 1. We see that our approximations differ from the exact result, but the difference decreases with increasing value of N. The 50-term approximation works reasonably well for all values of b for which the density differs appreciably from 0. Unfortunately the 10-, 20-, and 50-term approximations would require measurements at $Q^2 = 6, 23,$ and 144 GeV^2. Only the first value seems achievable at this time.

We now examine the dipole form factor given by

$$F_D(Q^2) = \frac{1}{\left(1 + \frac{Q^2}{\Lambda^2}\right)^2} \qquad (23)$$

where $\Lambda^2 = 0.71$ GeV^2. This value is suggested by its historically close relationship with the proton electromagnetic form factors. The dipole transverse charge density is obtained by from Eq. (1) to be

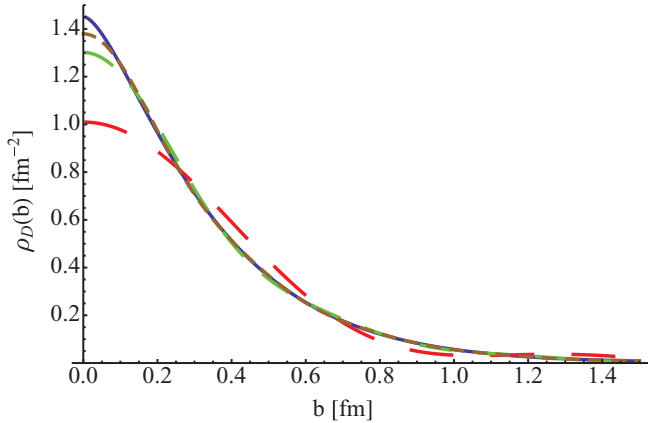$$\rho_D(b) = \frac{1}{4\pi} b \Lambda^3 K_1(b\Lambda). \qquad (24)$$

FIG. 2. (Color online) Plot of ρ_D (solid), 5-term approximation (red, long dash), 10-term approximation (green, medium dash), and 15-term approximation (brown, short dash).

TABLE I. Upper limit, N, dependence of $\langle b^2 \rangle_{M,D}$ computed for values of b from 0 to 1.5 fm.

N	$\langle b^2 \rangle_M$ (fm)^2	$\langle b^2 \rangle_D$ (fm)^2
5	0.259	0.313
10	0.362	0.320
15	0.368	0.319
∞	0.367	0.319

This form factor falls more rapidly with increasing Q^2 than does F_M and also corresponds to the larger physical extent of the proton as compared to the pion. Furthermore, ρ_D is not singular at the origin [$\sim 1 - 0.058(b\Lambda)^2$]. Thus, there are several reasons to expect to find better convergence properties and therefore a more accurate representation of the transverse density for the proton. With this value of Λ, $\langle b^2 \rangle = 8/\Lambda^2 = 0.439$ fm^2, and $R = 3.31$ fm. Once again the fractional difference of Eq. (12) is truly tiny for all values of n: The fractional differences are less than about 10^{-5} for all values of n that correspond to nonzero c_n. We plot ρ_D and its approximations in Fig. 2.

We can see how the approximations converge to the exact ρ_D. Even the 10-term approximation is reasonably good, and the 15-term approximation is extremely accurate except for $b < 0.1$ fm.

Another way of looking at convergence properties is to examine properties of the transverse density. We display upper-limit dependence of $\langle b^2 \rangle_{M,D}$ for both the monopole and dipole form factors. We compute these matrix elements for a range of values of b from 0 to 1.5 fm. This covers the region up to where ρ is about 0.1% of its central value. The results are shown in Table I. Despite the relatively poor convergence obtained for the monopole form factor (Fig. 1), reasonable convergence for the expectation value is obtained.

However, the convergence is much better for the dipole form factors. The 5-, 10-, and 15-term approximations correspond to values of $Q^2 = 0.9, 4,$ and 9 GeV^2. These and even greater values have already been achieved experimentally. Thus, we reasonably expect that the proton transverse density is now known. Indeed, this has already been suggested [9]. Thus, now we can answer the question: 'How well is the proton transverse charge density known?'

IV. EXTRACTION OF PROTON FORM FACTORS AND UNCERTAINTIES

The transverse densities we seek are given in terms of the Dirac F_1 and Pauli F_2 form factors, which are expressed in terms of the Sachs electromagnetic form factors G_E and G_M as

$$F_1(Q^2) = \frac{G_E + \tau G_M}{1 + \tau}, \quad F_2(Q^2) = \frac{G_M - G_E}{1 + \tau}, \qquad (25)$$

where $\tau = \frac{Q^2}{4M_p^2}$.

Elastic electron-proton scattering has been measured up to Q^2 of about 30 GeV^2, with the separation of both G_E and G_M extracted using a variety of techniques up to 10 GeV^2.

There are two sources of uncertainty in the extraction of the transverse densities. Experimental uncertainties from the measurements of G_E and G_M yield uncertainty in the extracted densities, and incompleteness errors arise from the lack of form factor measurements at very high Q^2 (above 30 GeV^2). In this section, we perform extractions of the transverse density and evaluate the effects that two kinds of uncertainties have on the densities.

The form factors G_E and G_M have been extracted from a global analysis of the world's cross-sectional and polarization data, including corrections for two-photon exchange corrections from Ref. [18]. The analysis is largely identical to that that of Ref. [19], although additional high-Q^2 form factor results [20] have been included. In addition, the slopes of G_E and G_M at $Q^2 = 0$ were constrained in the global fit based on a dedicated analysis of the low-Q^2 data. In the global fit, the large body of high-Q^2 data, especially for G_M, can constrain the fit well enough that the low-Q^2 behavior is not primarily constrained by the low-Q^2 data. Constraining the slope based on an analysis of only the low-Q^2 data keeps the global fit from doing a poor job at low Q^2 simply to make a slight improvement in the high-Q^2 data. In writing $G_E(Q^2) = 1 - Q^2 R_E^2/6$, the value of R_E was constrained to be 0.878 fm, and R_M was constrained to be 0.860 fm. This is important in the extraction of the large-scale structure of the density. The fit is of the following form:

$$G_M(Q^2) = \mu_p \frac{1 + p_6\tau + p_{10}\tau^2 + p_{14}\tau^3}{1 + p_2\tau + p_4\tau^2 + p_8\tau^3 + p_{12}\tau^4 + p_{16}\tau^5},$$

$$G_E(Q^2) = \frac{1 + q_6\tau + q_{10}\tau^2 + q_{14}\tau^3}{1 + q_2\tau + q_4\tau^2 + q_8\tau^3 + q_{12}\tau^4 + q_{16}\tau^5}, \quad (26)$$

where the fitting constants $p_2 \ldots p_{16}, q_2 \ldots q_{16}$ are given in Table II and we use $\mu_p = 2.792782$.

We also need a reliable estimate of the experimental uncertainties in the form factors to determine the uncertainty in the extracted coefficients $\tilde{c}_n$. In the global analysis, there are two sources that can contribute to the uncertainties in G_E and G_M: the uncertainty on each individual cross section or polarization ratio and the normalization uncertainty associated with each cross section data set. The normalization factors are allowed to vary in the fit, as was the case in Ref. [19]. To estimate the uncertainty in the fitted normalization factors, we take the normalization factor from a single data set and vary it around its best fit value (while allowing all other parameters to vary) to map out the change in the χ^2 of the fit as a function

TABLE II. Fit parameters for G_M (p_i) and G_E (q_i).

i	p_i	q_i
2	9.70703681	14.5187212
4	3.7357×10^{-4}	40.88333
6	-1.43573	2.90966
8	6.0×10^{-8}	99.999998
10	1.19052066	-1.11542229
12	9.9527277	4.579×10^{-5}
14	2.5455841×10^{-1}	3.866171×10^{-2}
16	12.7977739	10.3580447

of the normalization factor. This yields uncertainties between 0.2% and 2.5% (typically 0.6%–1%), compared to the initially quoted uncertainties of 1.5% to 5%, for the data before the normalization has been constrained by the fit. However, by assuming that all uncertainties are entirely uncorrelated or pure normalization factors, we neglect the possibility that there may be some angle-dependent or Q^2-dependent correction that could bias the determination of the relative normalization coefficients. Thus, we assume that the final uncertainty on each normalization factor is at least 0.5%, even if the result of the χ^2 analysis yields a smaller result.

Having the uncorrelated uncertainties for each data point and the constrained normalization uncertainties, we then extract the uncertainties for G_E and G_M. For the uncorrelated uncertainties, we randomly shift each cross section and polarization ratio measurement within its uncertainties and then redo the fit for G_E and G_M. We repeat this 1000 times and look at the range of values for several Q^2 values (55 Q^2 values between 0.007 and 31.2 GeV^2). This yields our uncorrelated uncertainty at each of the Q^2 points. To obtain the impact of the normalization uncertainties, we repeat this procedure, varying the normalization of each cross-sectional data set according to its uncertainty and determine the range of G_E, G_M values for the same set of Q^2 points. In this procedure, the uncertainty obtained depends on the fit function used, and a functional form with insufficient flexibility will yield significant smoothing of the results and thus unrealistically small uncertainties. We scale up our uncertainties by a factor of two, which yields good agreement with best direct measurements of the form factors and uncertainties.

As mentioned previously, we use the electric and magnetic radii extracted from just the low-Q^2 data in as a constraint to the global fit, which can yield unrealistically small uncertainties for below $Q^2 = 0.2$ GeV^2, especially for G_M, where the very low Q^2 data is extremely limited. Thus, for these low Q^2 values, we calculate the uncertainty at each Q^2 corresponding to the uncertainty in the extracted radius, assuming the linear expansion. We take this larger uncertainty, rather than the result from the fit, until the uncertainties from direct extractions of the form factors are of comparable size, at which point we take the direct extraction of the uncertainty. For $Q^2 > 10$ GeV^2, there are no direct extractions of G_E, and thus we again have to be sure that we do not underestimate the uncertainties. The global fit yields $G_E/G_D \approx 0$ at high Q^2, but it is difficult to tell if G_E becomes zero or if G_E/G_M continues its linear decrease with Q^2 [20]. Thus, for $Q^2 > 10$ GeV^2, we set the uncertainty to be the difference between the best fit, which yields $G_E \approx 0$, and the fit where the linear falloff in G_E/G_M continues, with G_E changing sign and then increasing in absolute value.

We then use the fit and uncertainties for G_E and G_M to extract F_1 and F_2, treating the uncertainties in G_E and G_M as uncorrelated, yielding

$$(dF_1)^2 = \left(\frac{1}{1+\tau}\right)^2 (dG_E)^2 + \left(\frac{\tau}{1+\tau}\right)^2 (dG_M)^2, \quad (27)$$

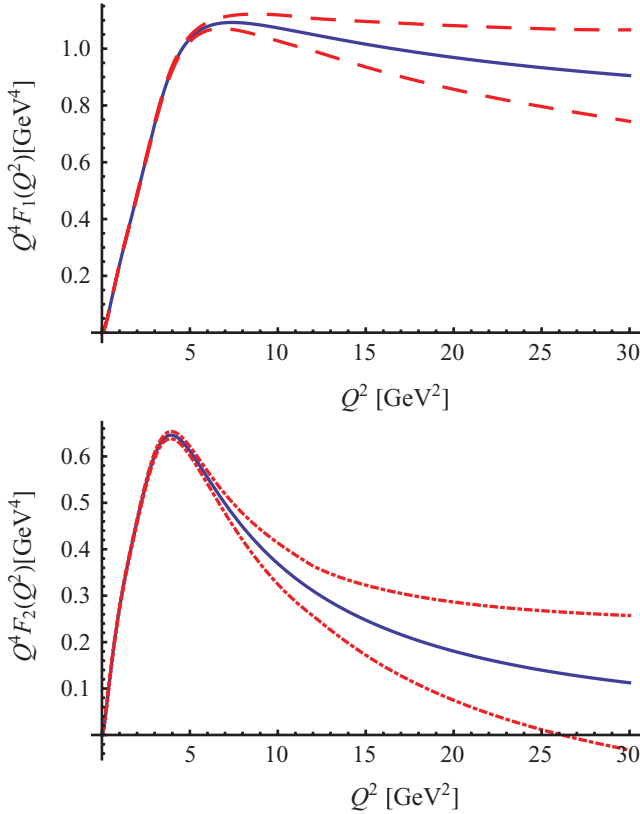$$(dF_2)^2 = \left(\frac{1}{1+\tau}\right)^2 (dG_E)^2 + \left(\frac{1}{1+\tau}\right)^2 (dG_M)^2. \quad (28)$$

FIG. 3. (Color online) The electromagnetic form factors $F_1(Q^2)$ and $F_2(Q^2)$ and their error bands, scaled by a factor of Q^4.

While the Rosenbluth extractions yield a strong anticorrelation between the uncertainties on G_E and G_M, the polarization ratio yields a correlated uncertainty; in the global fit, the combined result is fairly well approximated by entirely uncorrelated uncertainties. Figure 3 shows the extracted values of F_1 and F_2 along with their uncertainties. Because the elastic cross section is dominated by the contribution from G_M at large Q^2, the fractional uncertainties on G_E are much larger, and the uncertainty on G_E dominates the uncertainty on both F_1 and F_2, even though its contribution to F_1 is suppressed by a factor of τ relative to the G_M contribution.

We note that for $Q^2 < 0.5$, the uncertainty coming from cross-sectional normalizations can be the larger contribution to the total uncertainty (and it is dominant for G_E below 0.1 GeV^2). While the normalization uncertainty in the cross sections will not give a normalization-style uncertainty on G_E, the normalization of a given experiment will tend to have a correlated effect on all of the extractions within the Q^2 covered by the experiment. This effect is accounted for by using the procedure discussed in Sec. V A.

V. EXTRACTION OF REALISTIC PROTON TRANSVERSE DENSITIES

The principle aim of this paper is to use data observed in experiments to obtain the charge and magnetization densities.

Recall that the transverse charge density ρ_{ch} is given by

$$\rho_{ch}(b) = \frac{1}{2\pi} \int Q \, dQ \, J_0(Qb) F_1(Q^2). \tag{29}$$

The two-dimensional Fourier transform of F_2, ρ_2 is similarly given by

$$\rho_2(b) = \frac{1}{2\pi} \int Q \, dQ \, J_0(Qb) F_2(Q^2). \tag{30}$$

However, the true magnetization density, obtained by computing the expectation value of the transverse position operator with the electromagnetic current operator, is given [10] by

$$\rho_M(b) = -b \frac{d}{db} \rho_2(b)$$
$$= \frac{b}{2\pi} \int Q^2 \, dQ \, J_1(Qb) F_2(Q^2). \tag{31}$$

This quantity is the density related to the anomalous magnetic moment. We begin by extracting $\rho_{ch,2}$. The starting point is to use these expressions along with the experimentally determined $F_{1,2}$ obtained from the fits of Sec. IV. However, extracting realistic transverse densities requires a determination of the uncertainties in the results. There are two sources of uncertainty. Experimental data have uncertainties in the region where they are measured, and no direct information is available above some maximum value of $Q^2 = Q^2_{max}$, where there are no measurements. The experimental uncertainties lead directly to uncertainties in the $\widetilde{c}_n$ via Eq. (3), and can be taken into account without further ado. However, uncertainty must arise because of lack of knowledge of form factors for $Q^2 > Q^2_{max}$, and these need to be estimated. This error is called the incompleteness error.

A. Impact of experimental uncertainties on the extracted transverse densities

We first treat the experimental uncertainties. We use only the series Eq. (5) for values of Q^2_n for which form factors have been extracted. The magnetic form factor G_M is well measured up to $Q^2 = 31$ GeV^2, but G_E is only known up to ~ 10 GeV^2. Based on the estimated uncertainties on G_E above 10 GeV^2, we find that while F_1 is relatively well measured up to 30 GeV^2, the uncertainties on F_2 grow rapidly above 10 GeV^2, reaching 25% by 13 GeV^2. These upper limits on Q^2 are related to limits on the summation index n [of Eq. (5)] through Eq. (4), which requires values of R_i. Taking $\langle b^2 \rangle$ given by $\rho_{ch,2}$ from the fits presented previously, we use Eq. (17) to obtain $R_1 = 3.29$ fm and $R_2 = 3.62$ fm for $F_{1,2}$. This corresponds to upper limits N on the sum over n: $n = 30$, $Q^2_{30} = 31$ GeV^2 for $\rho_{ch}(b)$, but only up to $n = 20$, $Q^2_{20} = 11$ GeV^2 for $\rho_2(b)$.

The transverse densities $\rho_{ch,2}$ are plotted as the solid curves in Fig. 4. The densities peak at $b = 0$ and the transverse density ρ_2 has a slightly broader spatial extent than that of ρ_{ch}.

The next step is to extract $\widetilde{c}_n$ from the fit to the form factor using Eq. (3). The uncertainty on $F_{1,2}(Q^2)$ directly yields an uncertainty on $\widetilde{c}_n$ and thus its contribution to $\rho(b)$ [Eq. (2)]. Assuming the errors from each $\widetilde{c}_n$ extraction add
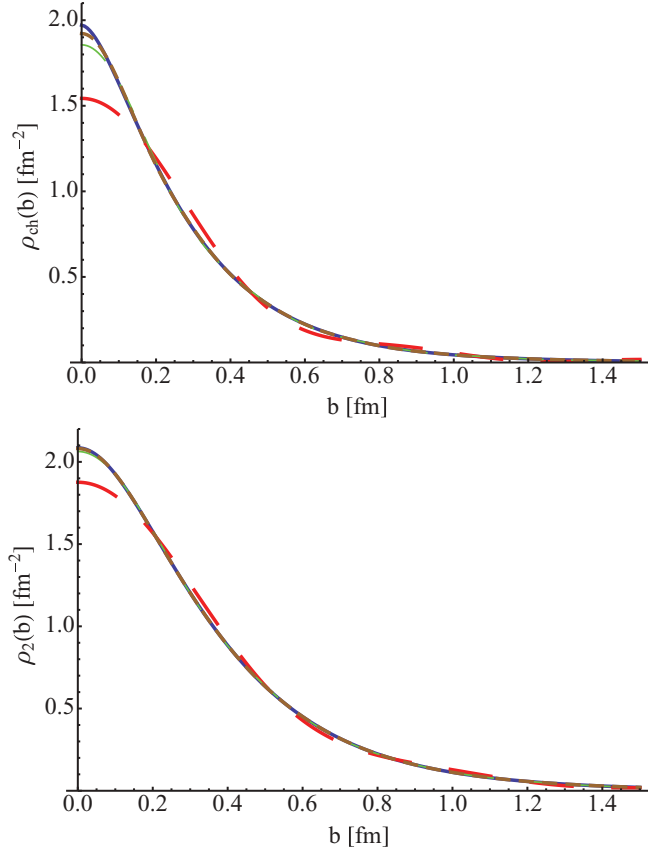
FIG. 4. (Color online) The transverse densities ρ_{ch}, ρ_2 (blue, solid) of the parametrizations and their approximates to 10 terms (red, long dash), 20 terms (green, medium dash), 30 terms (brown, short dash) using the parametrization of Eq. (26). The approximations converge as the number of terms increases.

constructively, we obtain

$$\Delta_{\text{exp}}\rho_{\text{ch}}(b) = \sum_{n=1}^{30} \left| \frac{\partial \rho_{\text{ch}}(b)}{\partial F_1} \right| dF_1\left[\left(\frac{X_n}{R_1} \right)^2 \right]$$

$$= \frac{1}{\pi R_1^2} \sum_{n=1}^{30} J_1(X_n)^{-2} \left| J_0\left(X_n \frac{b}{R_1} \right) \right| dF_1\left[\left(\frac{X_n}{R_1} \right)^2 \right],$$

$$(32)$$

$$\Delta_{\text{exp}}\rho_2(b) = \sum_{n=1}^{20} \left| \frac{\partial \rho_2(b)}{\partial F_2} \right| dF_2\left[\left(\frac{X_n}{R_2} \right)^2 \right]$$

$$= \frac{1}{\pi R_2^2} \sum_{n=1}^{20} J_1(X_n)^{-2} \left| J_0\left(X_n \frac{b}{R_2} \right) \right| dF_2\left[\left(\frac{X_n}{R_2} \right)^2 \right].$$

$$(33)$$

Note that the errors are added linearly. This means that we are taking the worst case possible by assuming a full correlation. These uncertainties in densities are plotted in Fig. 5. They are about 1.5% of the transverse density at $b = 0$ and decrease (in absolute value) at increasing distances. The fractional uncertainty is small (less than 10%) until $b \approx 1$ fm, where the density is only a few percent of the peak density.
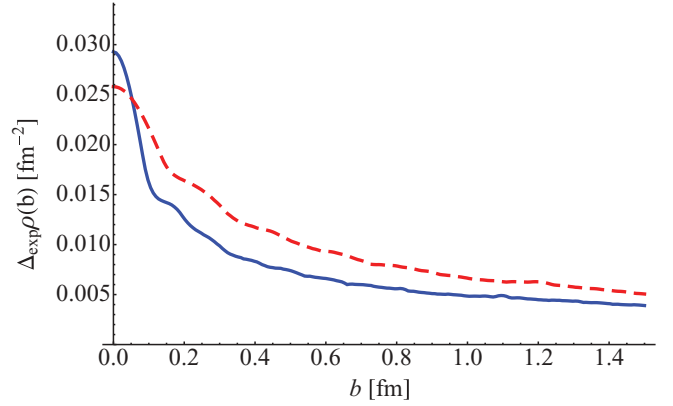

FIG. 5. (Color online) Uncertainties in transverse densities $\Delta_{\text{exp}}\rho_{\text{ch}}$ (solid, blue) and $\Delta_{\text{exp}}\rho_2(b)$ (dashed, red) due to experimental uncertainties on F_1, F_2.

B. Incompleteness error

We next study the uncertainties in the transverse density caused by lack of experimental knowledge at large values of Q^2. The first step is to understand the meaning of the truncations made in Eqs. (29) and (31). Plots of these approximations are given in Fig. 4. We see that for ρ_2 one achieves agreement with the parametrization for values of N as low as 20, with the largest disagreement at $b = 0$. For $\rho_{\text{ch}}(b = 0)$, the difference between the result from the parametrization and the $N = 30$ approximation is -2%, while for $\rho_2(b = 0)$, the $N = 20$ approximation is only 1% below the full result. Even though fewer terms are included in the approximation for F_2, the agreement is comparable because of the more rapid fall-off of F_2 with increasing values of Q^2.

Given this information, we can state our procedure. Our basic transverse densities are obtained by using the parametrization Eq. (26) to evaluate the expressions of Eqs. (29), (30), and (31). However, we are justified in using this parametrization for values of Q^2 corresponding to $N = 30$ (20) for $F_{1(2)}$. We assume a maximum error by taking the uncertainty in the form factor to be $\pm$ the value given by the parametrization. Therefore, the estimated incompleteness uncertainty is given
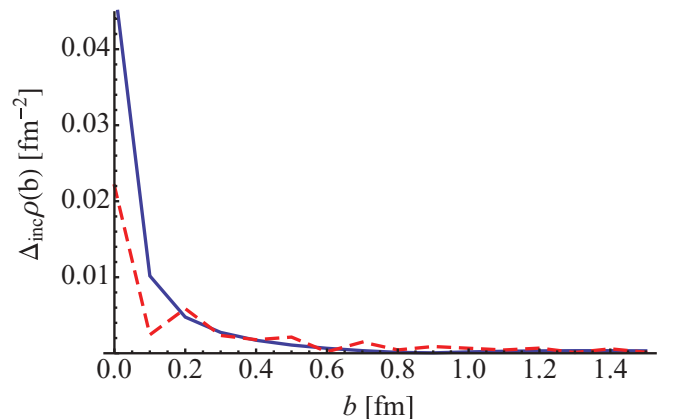

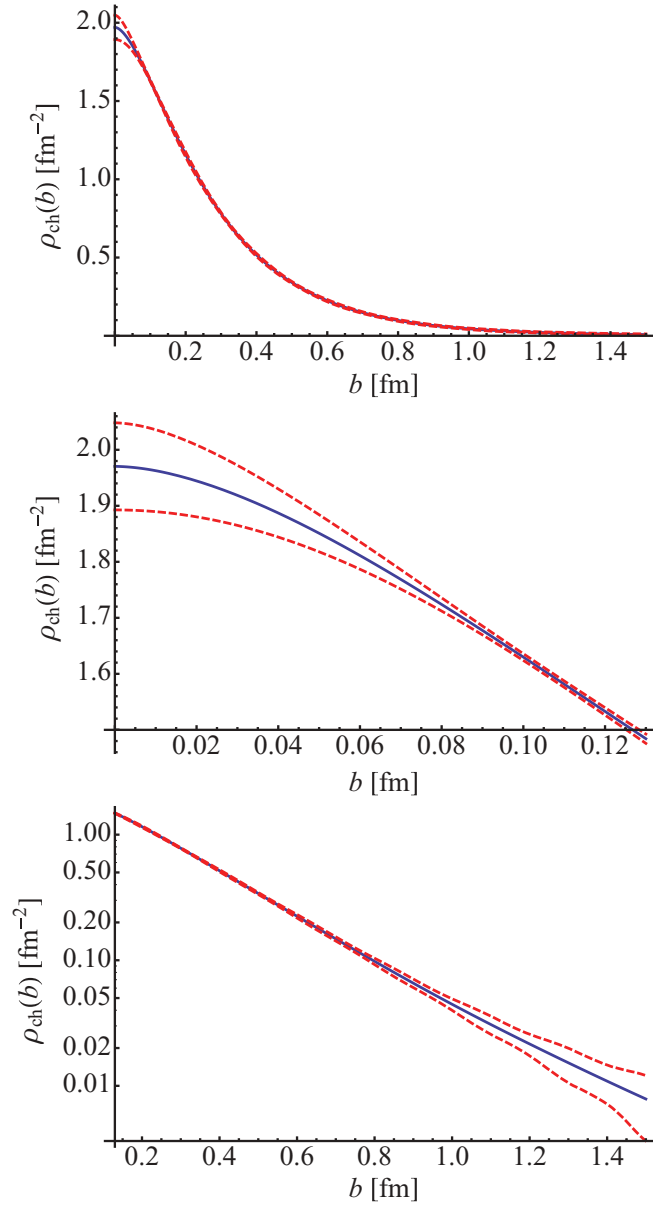FIG. 6. (Color online) Incompleteness error. The absolute error in ρ_{ch} (solid, blue) and ρ_2 (dashed, red).

FIG. 7. (Color online) ρ_{ch} (solid, blue) with error bands (short dashed, red).

FIG. 8. (Color online) ρ_2, with error bands.

by the expression

$$\Delta_{\text{inc}}(b) \equiv \left| \sum_{N+1}^{\infty} c_n J_0(X_n/R_1) F_i \left(Q_n^2 \right) \right|, \quad (34)$$

as a function of b, with $i = 1, 2$. The results are shown in Fig. 6. It is necessary to realize that using this expression for the incompleteness error overestimates the error because using this expression is equivalent to assuming that the form factor vanishes for $Q^2 > Q_N^2$ in Eq. (5). But the form factor cannot suddenly drop to 0. Figure 3 shows a fractional error bar for F_1 (31 GeV^2) that is only about 0.2 and a fractional error bar at 13 GeV^2 that is only about 0.3 of the form factor F_2. Thus, using Eq. (34) amounts to making an overestimate. To be conservative, we obtain the total uncertainty by adding
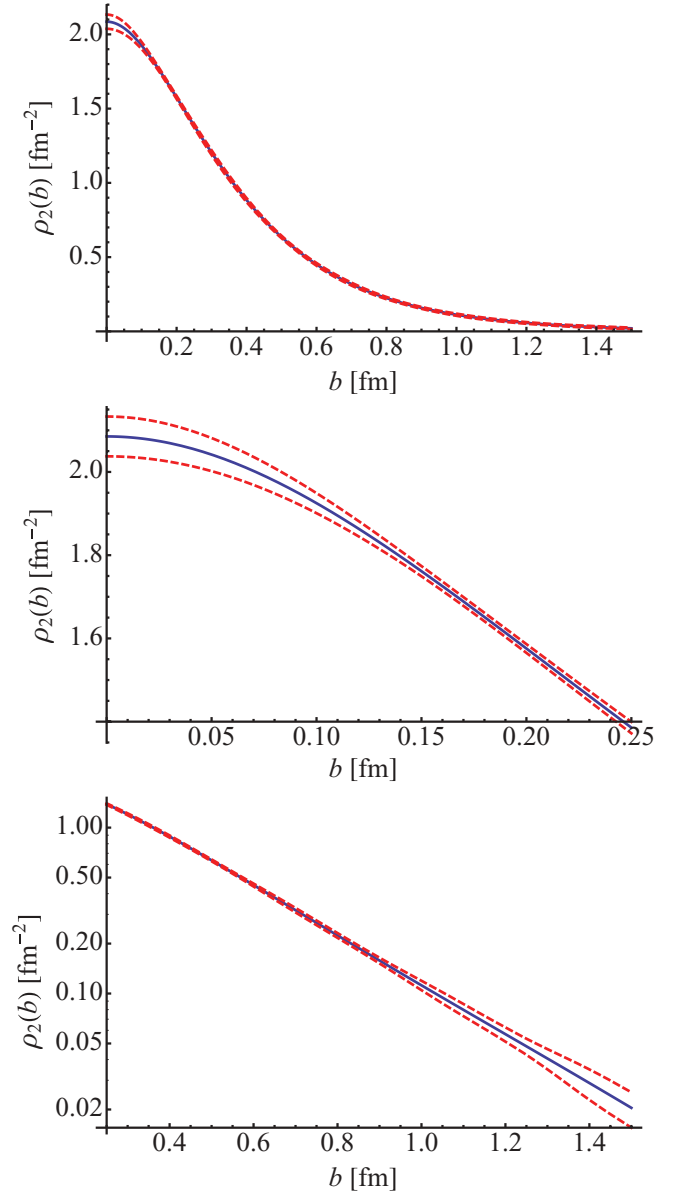
the contributions of Eq. (32) [or Eq. (33)] to the estimated incompleteness uncertainty given by Eq. (34).

We now have working expressions for the transverse densities $\rho_{\text{ch},2}$ and their respective uncertainties. We start with the basic term for $\rho_{\text{ch},2}$, obtained by using the parametrization Eq. (26) to evaluate the expressions of Eqs. (29), (30), and (31), then add the two separate errors $\Delta_{\text{inc,exp}}$ to get a total error $\Delta = \Delta_{\text{inc}} + \Delta_{\text{exp}}$ for ρ_{ch}. A band is formed by considering the region between the basic plus or minus the appropriate Δ for the two densities.

The transverse densities $\rho_{\text{ch},2}(b)$ are plotted with their error bands in Figs. 7 and 8. The errors are very small except for values of b less than about 0.1 fm. The results in this figure are the central numerical findings of this paper. The transverse densities are known very well indeed. The spatial extent of ρ_2 is broader than that of ρ_{ch} as previously observed [21]. Note
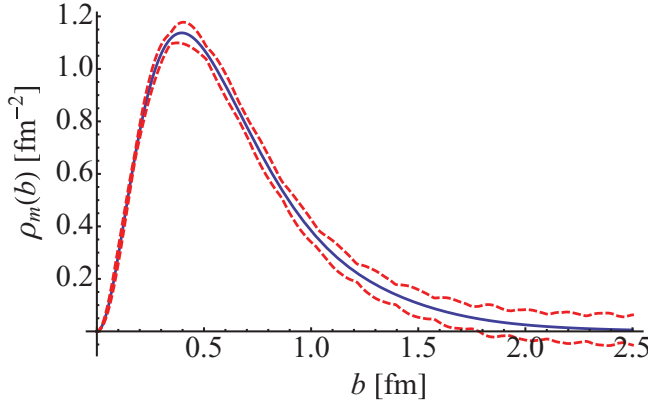
FIG. 9. (Color online) True magnetization density ρ_m. The uncertainties are numerically negligible.

that the realistic transverse densities differ substantially from the dipole result of Eq. (24), shown in Fig. 2.

C. Extraction of $\rho_M(b)$

We now turn to the true transverse anomalous magnetic density of Eq. (31), defined by taking the matrix element of $\frac{1}{2}\int d^3r(\mathbf{b}\times\vec{j})$ in a transversely polarized state [10,21]. This Fourier transform involves $J_1(Qb)$, and therefore the FRA corresponds to that of Eqs. (19) and (20), with $\lambda = 1$. Using this expansion, instead of simply taking the derivative of ρ_2, allows an expansion in basis functions that explicitly vanish at $b = R_2$. Then the FRA gives the result

$$\rho_M = \frac{1}{\pi R_2^2}\sum_{n=1}^{\infty}J_2^{-2}(X_{1,n})bQ_{1,n}F_2\left(Q_{1,n}^2\right)J_1(Q_{1,n}b),$$

$$Q_{1,n}\equiv\frac{X_{1,n}}{R_2}. \tag{35}$$

Once again, we include the effects of the experimental error and the incompleteness error. This latter error is larger in

this case than for ρ_2 because of the explicit factor of $X_{1,n}$. The results for ρ_m and its error bands are plotted in Fig. 9. This quantity has a broader spatial extent than ρ_2, possibly resulting from the importance of the pion cloud in causing the anomalous magnetic moment. The uncertainties on this quantity are greater than for the other densities. Future measurements extending knowledge of F_2 to higher values of Q^2 would reduce these higher uncertainties.

VI. SUMMARY

This paper is concerned with obtaining a general method to determine information about densities in the transverse plane. The use of Bessel series expansion, augmented by the FRA of Eqs. (2), (3), (19), and (20), allows us to determine the effects of experimental uncertainties and also allows us to estimate the effects of the incompleteness error caused by a lack of measurements at large values of Q^2. The method can be applied to the extraction of any spatial quantity. One example, related to orbital angular momentum, is shown in Eqs. (19) and (20).

The method is applied here to analyze electromagnetic form factors. We can see from Figs. 7 and 8 that the errors associated with the transverse charge density and the two-dimensional Fourier transform of F_2 are very small. The anomalous magnetization density ρ_M, Fig. 9, is also reasonably well determined, but future measurements extending our knowledge of F_2 to higher values of Q^2 would reduce the existing uncertainties.

[1] H. Y. Gao, Int. J. Mod. Phys. E **12**, 1 (2003); **12**, 567(E) (2003).
[2] C. E. Hyde and K. de Jager, Annu. Rev. Nucl. Part. Sci. **54**, 217 (2004).
[3] C. F. Perdrisat, V. Punjabi, and M. Vanderhaeghen, Prog. Part. Nucl. Phys. **59**, 694 (2007).
[4] J. Arrington, C. D. Roberts, and J. M. Zanotti, J. Phys. G **34**, S23 (2007).
[5] T. Horn *et al.*, Phys. Rev. C **78**, 058201 (2008).
[6] H. P. Blok *et al.* (Jefferson Lab Collaboration), Phys. Rev. C **78**, 045202 (2008).
[7] R. Hofstadter, Rev. Mod. Phys. **28**, 214 (1956).
[8] G. A. Miller, Phys. Rev. C **80**, 045210 (2009).
[9] G. A. Miller, Phys. Rev. Lett. **99**, 112001 (2007).
[10] G. A. Miller, Annu. Rev. Nucl. Part. Sci. **60**, 1 (2010).
[11] M. Burkardt, Phys. Rev. D **62**, 071503 (2000); **66**, 119903(E) (2002); Int. J. Mod. Phys. A **18**, 173 (2003).
[12] M. Diehl, Eur. Phys. J. C **25**, 223 (2002); **31**, 277(E) (2003).
[13] V. D. Burkert, arXiv:0810.4718 [hep-ph].
[14] H. Nyquist, Trans. Amer. Inst. Elect. Eng. **47**, 617 (1928); C. E. Shannon, Proc. IRE **37**, 10 (1949).
[15] D. E. Soper, Phys. Rev. D **15**, 1141 (1977).
[16] M. Strikman and C. Weiss, Phys. Rev. C **82**, 042201 (2010).
[17] J. D. Jackson, *Classical Electrodynamics*, 3rd ed. (Wiley, New York, 1998).
[18] P. G. Blunden, W. Melnitchouk, and J. A. Tjon, Phys. Rev. C **72**, 034612 (2005).
[19] J. Arrington, W. Melnitchouk, and J. A. Tjon, Phys. Rev. C **76**, 035205 (2007).
[20] A. J. R. Puckett *et al.*, Phys. Rev. Lett. **104**, 242301 (2010).
[21] G. A. Miller, E. Piasetzky, and G. Ron, Phys. Rev. Lett. **101**, 082002 (2008).